Supplementary Information

Lead-free hybrid piezoelectric ceramic stack for both potent and temperature-stable piezoelectricity

Kyu-Hyun Park, [1] Min-Ku Lee,[1] Byung-Hoon Kim, Changyeon Baek, Gyoung-Ja Lee[*]

Nuclear System Integrity Sensing & Diagnosis Division, Korea Atomic Energy Research Institute, 111 Daedeok-daero, 989 Beon-gil, Yuseong-gu, Daejeon, 34057, Republic of Korea

[1] K.-H. Park and M.-K. Lee equally contributed to this work.

[*] Correspondence: leegj@kaeri.re.kr (G.-J. Lee); Tel: +82-42-868-4838

[Contents]

Note 1. Structural properties of sintered KNN-a ceramic by Rietveld refinement

Note 2. Electrical properties of lead-free KNN-a piezoceramic

Note 3. Structural properties of sintered BFBT-b ceramic by Rietveld refinement

**Note 4. Electrical properties of lead-free BFBT-b piezoceramic**

Note 5. Sensing performance characteristics of an accelerometer prototype built using lead-free piezoceramics

Note 6. Basic structure of a compression-mode piezoelectric accelerometer

Note 7. Experimental setup for high-temperature vibration monitoring tests

Note 1) Structural properties of sintered KNN-a ceramic by Rietveld refinement

The Rietveld refinement indicates that the ferroelectric R and T phases coexisted with a higher proportion of the T phase at 82%. The obtained low value of R_{wp} (= 8.94%) as well as S (= 1.56) close to 1 suggests high reliability of the refinement experiments.
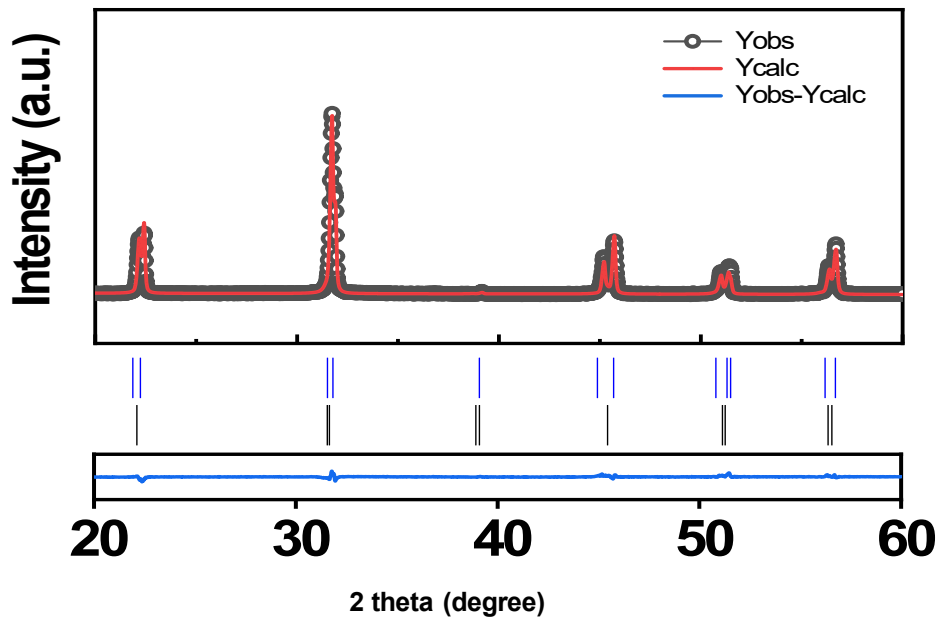
Material	Phase structure	Cell parameters			Phase Fraction (%)	R_{wp} (%)	S
		a(Å)	b(Å)	c(Å)			
KNN-a	R	3.9987	3.9987	3.9987	18 ($R3m$:R)	8.94	1.56
	T	3.9691	3.9691	4.0117	82 ($P4mm$)		

Figure S1. Rietveld refinement pattern and the resulting structural parameters including phase structure, cell parameters, quantitative phase fraction, reliability factor value R_{wp} and the goodness-of-fit indicator S.

Note 2) Electrical properties of lead-free KNN-a piezoceramic

Figure S2 shows temperature-dependent dielectric, ferroelectric and field-induced strain properties of KNN-a piezoceramic. The results indicate that all of ε_r, P_r and E-field induced

strains decrease, as the deviation from the optimal phase boundary region occurs with increasing temperature. Owing to a reduction in both intrinsic and extrinsic piezoelectricity activities, they are responsible for the changes in in-situ d_{33} and k_P with temperature.
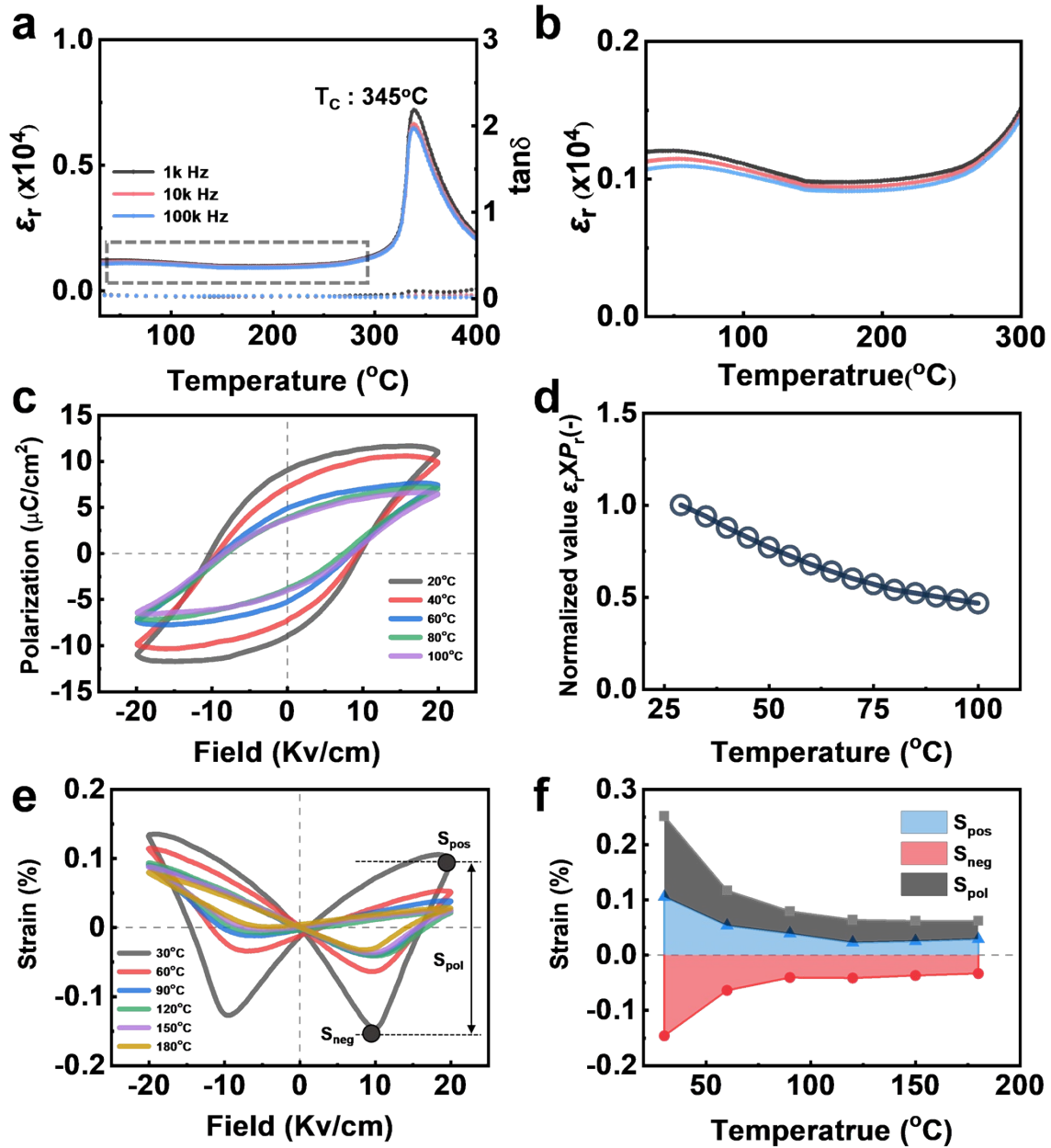

Figure S2. (a) Temperature-dependent ε_r and tanδ curves at different test frequencies (1, 10, 100 kHz) obtained from KNN-a piezoceramic. (b) ε_r-T curves between room temperature and 300 °C. (c) *P-E* loops with different temperatures. (d) Normalized $\varepsilon_r \times P_r$ behavior with temperature. (e) Bipolar *S-E* curves with different temperatures. (f) Temperature-dependent

strain behaviors of S_{pos}, S_{neg} and S_{pol}. S_{pos} is the highest strain value in the positive direction on the *S-E* curve, representing the sum of intrinsic lattice strain (S_{piezo}) and reversible (extrinsic) domain switching (S_{swich}). S_{neg} is the absolute value of the lowest strain in the negative direction, related to irreversible (extrinsic) non-180° domain switching. Poling strain (S_{pol}) is calculated as the sum of S_{pos} and $|S_{neg}|$.

Note 3) Structural properties of sintered BFBT-b ceramic by Rietveld refinement

The Rietveld refinement analysis revealed that the *R* and *PC* (pseudocubic) phases coexist, forming a MPB structure. The fractions of *R* and *PC* phases were 59 and 41 %, respectively. The obtained low value of R_{wp} (= 7.12%) as well as S (= 1.58) close to 1 suggests high reliability of the refinement experiments.
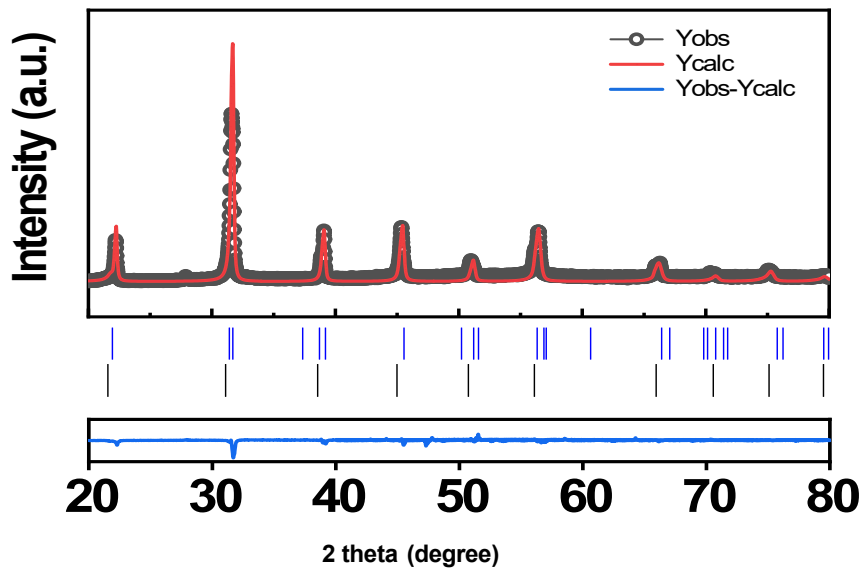
Material	Phase structure	Cell parameters			Phase fraction (%)	R_{wp} (%)	S
		a(Å)	b(Å)	c(Å)			
BFBT-b	R	5.6332	5.6332	13.8994	59 (*R3c*)	7.12	1.58
	PC	3.9943	3.9943	3.9943	41 (*Pm$\bar{3}$m*)		

Figure S3. Rietveld refinement pattern and the resulting structural parameters including phase structure, cell parameters, quantitative phase fraction, reliability factor value R_{wp} and the goodness-of-fit indicator S.

Note 4) Electrical properties of lead-free BFBT-b piezoceramic

Figure S4 shows temperature-dependent dielectric, ferroelectric and field-induced strain properties of BFBT-b piezoceramic. In contrast to the case of KNN-a, all of ε_r, P_r and E-field induced strains increase with increasing temperature, which are responsible for the real-time changes in d_{33} and k_P with temperature for BFBT-b piezoceramic.
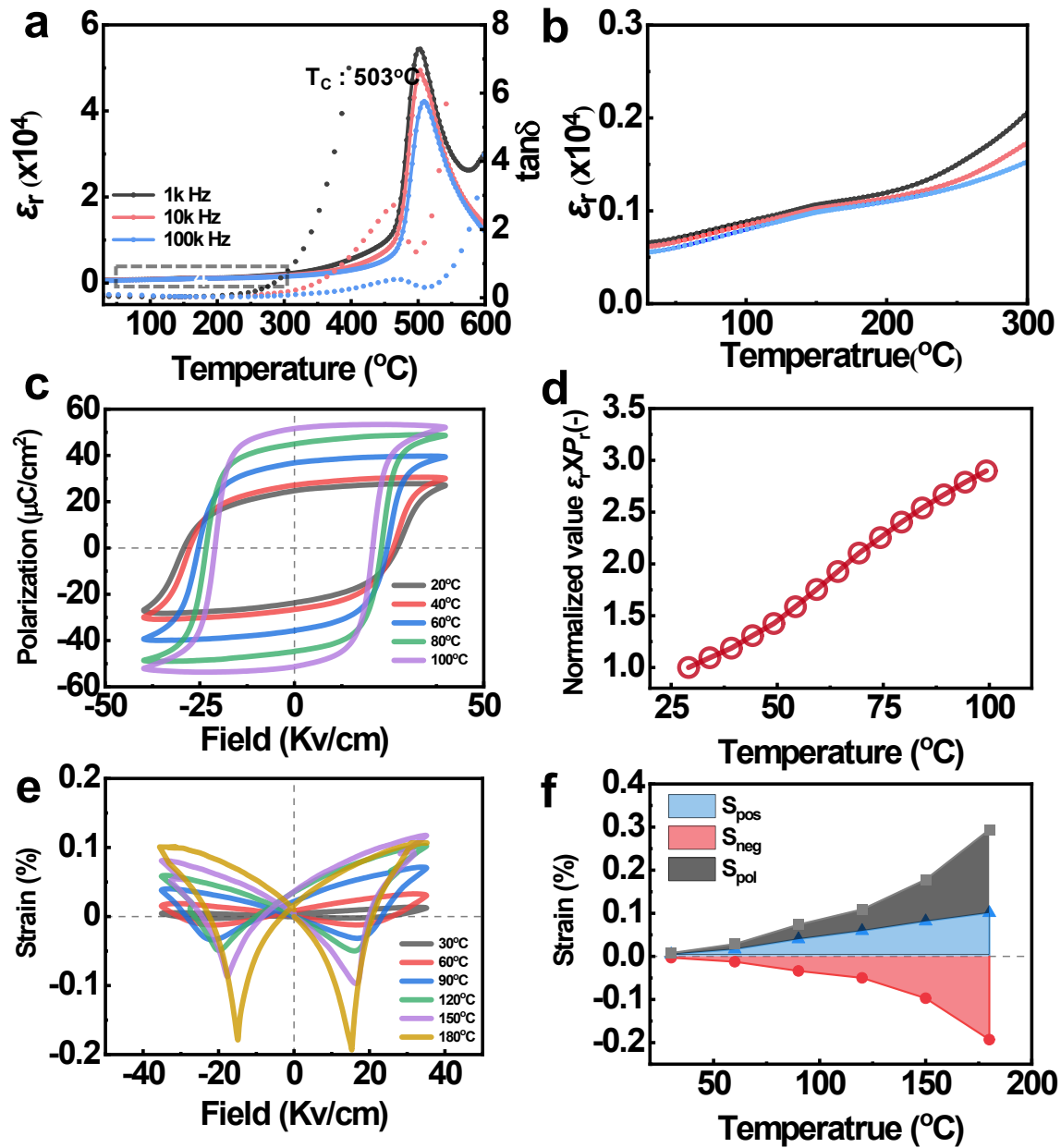
Figure S4. (a) Temperature-dependent ε_r and $\tan\delta$ curves at different test frequencies (1, 10, 100 kHz) obtained from BFBT-b piezoceramic. (b) ε_r-T curves between room temperature and 300 °C. (c) P-E loops with different temperatures. (d) Normalized $\varepsilon_r \times P_r$ behavior with temperature. (e) Bipolar S-E curves with different temperatures. (f) Temperature-dependent strain behaviors of S_{pos}, S_{neg} and S_{pol}. S_{pos} is the highest strain value in the positive direction on the S-E curve, representing the sum of intrinsic lattice strain (S_{piezo}) and reversible (extrinsic) domain switching (S_{swich}). S_{neg} is the absolute value of the lowest strain in the negative direction,

related to irreversible (extrinsic) non-180° domain switching. Poling strain (S_{pol}) is calculated as the sum of S_{pos} and $|S_{neg}|$.

Note 5) Sensing performance characteristics of an accelerometer prototype built using lead-free piezoceramics

The key performance indicators for developing a reliable accelerometer sensor are 1) the resonant frequency f_r and frequency response properties and 2) the linearity between the generated charge Q and the applied acceleration g. Therefore, both properties should be carefully checked and optimized after fabrication. As shown in Figure S5a, the high f_r of 23.4 kHz was obtained under mounted condition (i.e., attached condition). Since the f_r is very sensitive to the assembled condition and considered as a measure of reliability for the entire sensor assembly, such a high f_r value confirms high reliability of assembled sensor prototype, finally providing the capability of detecting signals across a broad frequency range. As shown in Figure S5b, it is also found that there is a perfect linearity between the generated Q and applied g with Pearson's correlation coefficient R (= 0.999) very close to "1". The excellent performances obtained from the sensor prototype fabricated under the optimized T_b condition are found comparable to those of commercial piezoelectric accelerometers, indicating that the sensor prototype was reliably produced.
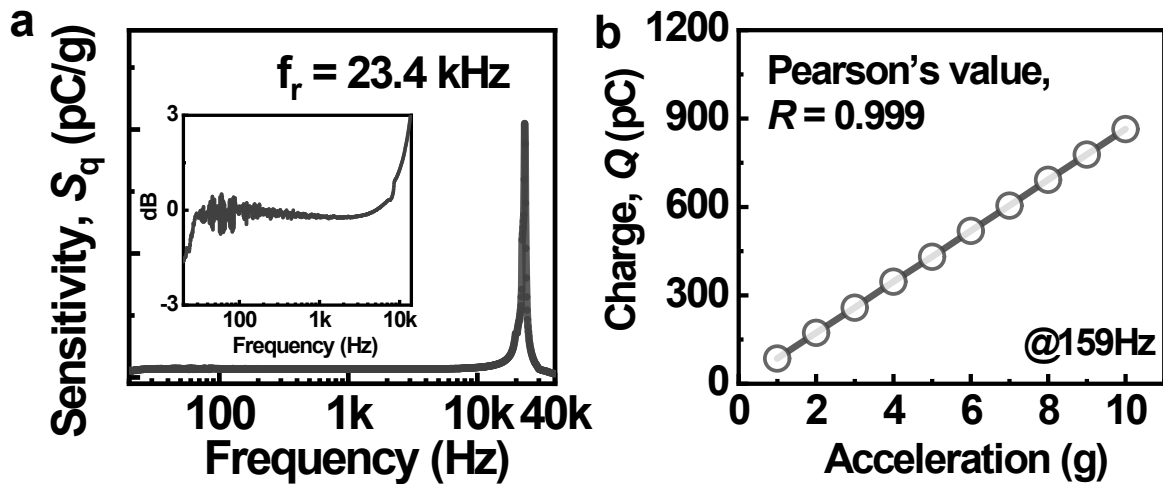
Figure S5. (a) Frequency response properties of the accelerometer prototype built using a lead-free KNN-a ceramic at the optimized T_b (= 196 N·cm). The inset represents an output signal converted into dB values. (b) Charge Q versus acceleration g measured for the corresponding accelerometer prototype at a test frequency of 159 Hz.

Note 6) Basic structure of a compression-mode piezoelectric accelerometer

Figure S6 shows the basic structure of a compression-mode piezoelectric accelerometer employed in this study. Importantly, appropriate torque load, T_b, is required to assemble all components reliably and achieve desired performances. The piezoelectric element consists of piezoceramic rings (1) cut for the longitudinal effect and oriented with their polarities opposite from the central electrode. The piezoceramic rings are connected electrically in parallel through electrodes (2) and mechanically in series. The poling direction of each cermic is indicated by arrows with respect to electrodes. All constituent components are preloaded under a compressive torque force between the head (seismic mass) (5) and base plate (6) by a bolt (3) and nut (4). The insulating layer (7) was inserted into the gap between the tail and the base plates. The electrode (2) captures the output signal and feeds it to the connector. When the base plate is accelerated, the seismic mass exerts a proportional force on the piezoceramic element.
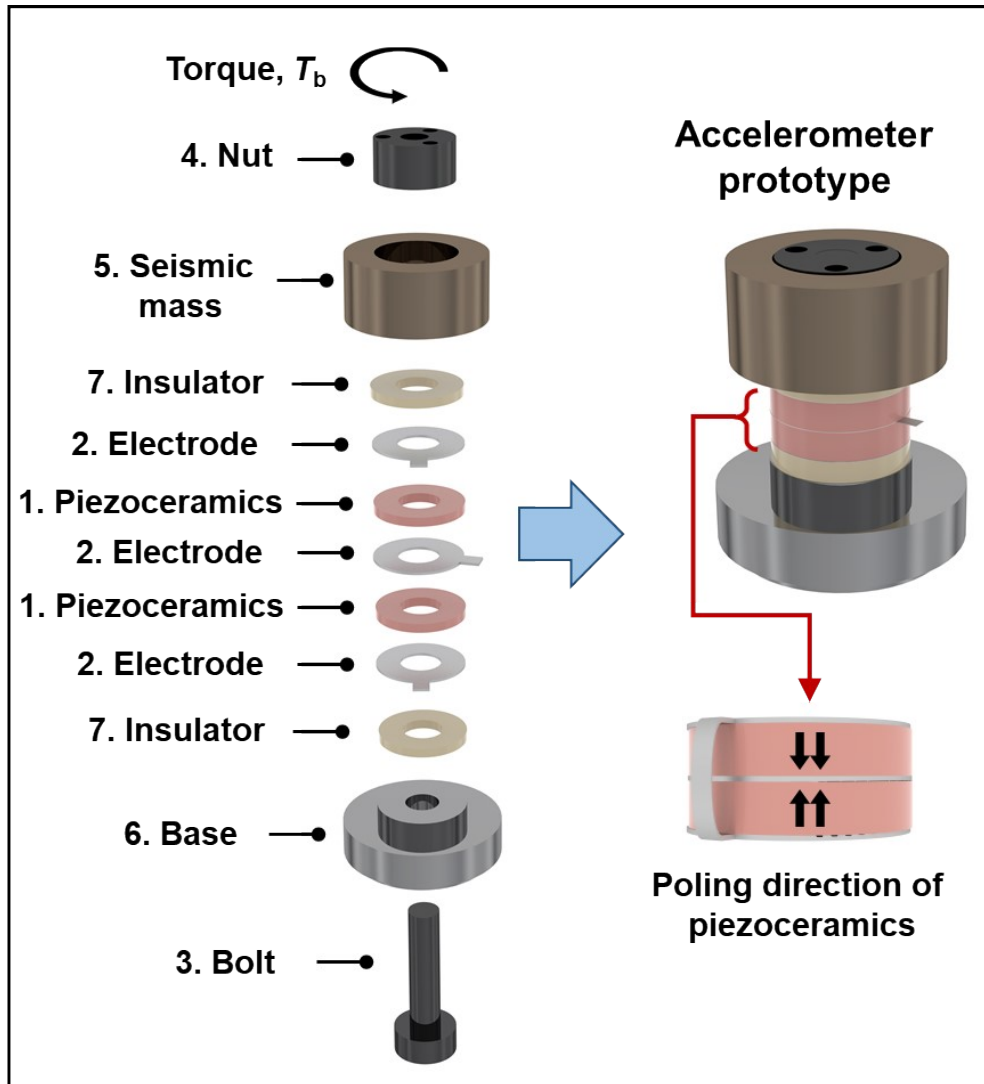
Figure S6. Exploded diagram showing a basic design and constituent components of a compression-mode accelerometer sensor (1: piezoceramic; 2: electrode; 3: bolt; 4: nut; 5: seismic mass; 6: base; 7: insulator) and an image showing a sensor prototype assembled using components and piezoceramics.

Note 7) Experimental setup for high-temperature vibration monitoring tests

Figure S7 shows a block diagram (left side) describing the experimental setup (right side) for high-temperature vibration monitoring test of the accelerometer prototypes built using lead-free piezoceramics. Details are described in Experimental section of the manuscript.
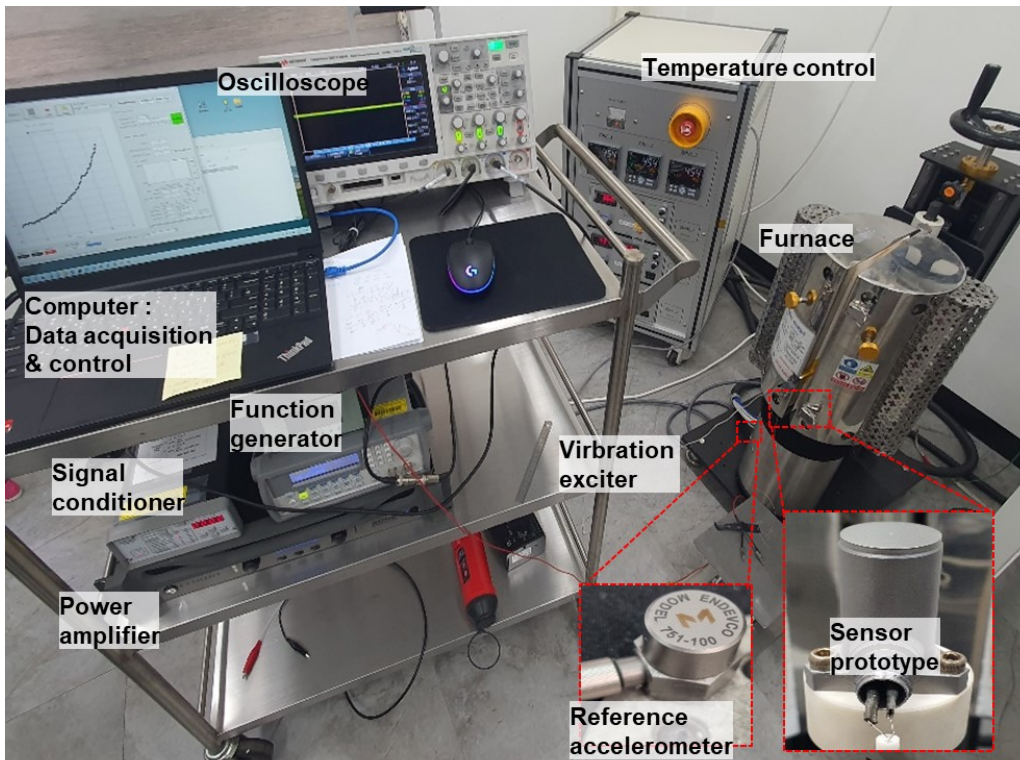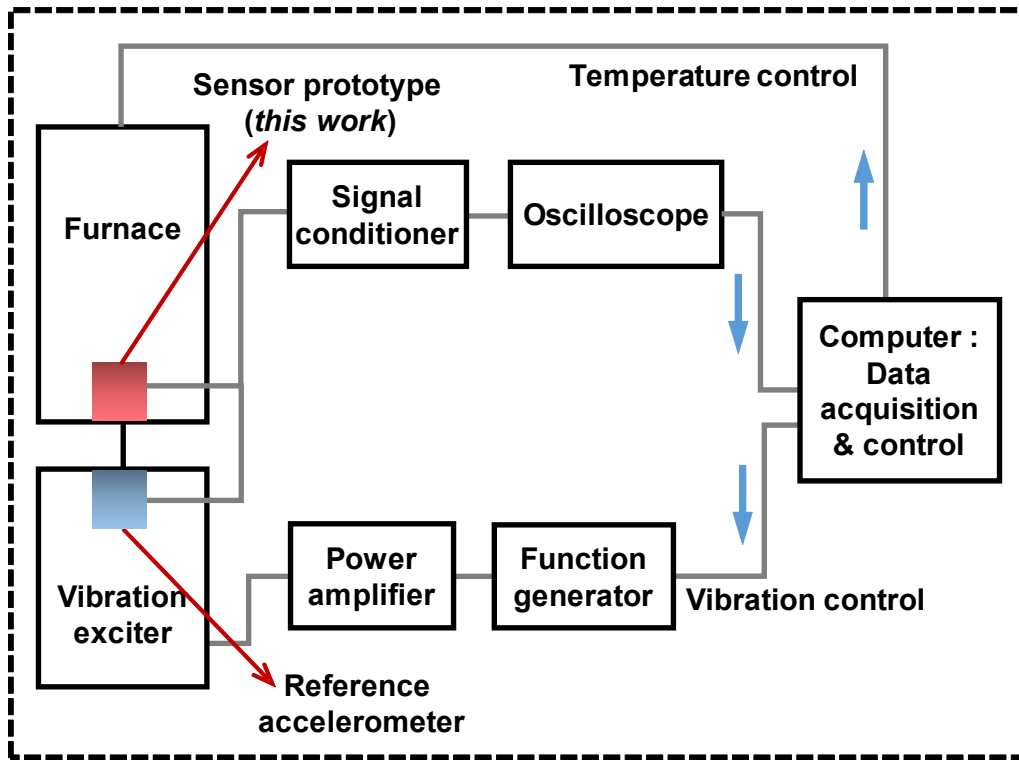
Figure S7. Block diagram of high-temperature vibration monitoring test (top) and a photo showing its whole experimental setup (bottom).